

Top-of-Atmosphere Flux Retrievals from CERES

Using Artificial Neural Networks

KONSTANTIN LOUKACHINE¹

Science Applications International Corporation, Hampton, Virginia

NORMAN G. LOEB

Center for Atmospheric Sciences, Hampton University, Hampton, Virginia

In print at
Remote Sensing of Environment
August 2004

¹ *Corresponding Author Address:* Dr. K. Loukachine, SAIC, One Enterprise Parkway, Suite 300, Hampton, VA 23666, U.S.A., e-mail: k.loukachine@larc.nasa.gov

1. Introduction

Long-term studies of the Earth’s radiation budget play an important role in understanding our planet, the impact of human activity on its climate, and detecting global climate change. As a part of the National Aeronautics and Space Administration (NASA) Earth-Observing System (EOS), The Clouds and the Earth’s Radiant Energy System (CERES) is designed to provide a precise record of top-of-atmosphere (TOA) reflected solar and emitted thermal radiative flux values, Wielicki et al. (1996). CERES measures shortwave (SW), longwave (LW), and window (WN) radiances over 20-km footprint (at nadir). To convert the measured radiances to TOA fluxes, Angular Distribution Models (ADMs) that depend on viewing geometry, surface type and atmospheric conditions are used. An ADM is defined as a collection of anisotropic correction factors for a specific scene type and depends explicitly on viewing geometry. Detailed scene identification (ID) over a CERES field-of-view is based on coincident retrievals from the Moderate-resolution Imaging Spectroradiometer (MODIS) measurements, Minnis et al. (2003). For CERES field-of-views with sufficient imager information, the ADMs are developed empirically, Loeb et al. (2004), and they are explicitly dependent on imager-derived cloud properties. However, the CERES/*Terra* dataset includes about 5.6% of CERES footprints with missing imager information or insufficient MODIS data for a reliable scene ID. The frequency of occurrence of these fields-of-view depends on imager viewing geometry, geographic location, and on certain cloud conditions, Minnis et al. (1999) and Minnis et al. (2003), and can reach up to 50% of data locally or for a specific scene type. In order to avoid any systematic bias in radiative budget data, it is very important to provide accurate TOA flux values for such footprints. This requires ADMs that can be used with the CERES measurements alone.

Empirical ADMs based only on radiometer geometry and broadband radiance measurements were developed for the Earth Radiation Budget Experiment (ERBE), Barkstrom (1984). These models are currently used for producing the ERBE-like datasets from the CERES measurements to provide a long-term record of radiation budget data. A method based on combination of theoretical simulation, narrow- and broadband radiance measurements was proposed by Stubenrauch et al. (1993) for obtaining LW anisotropic correction factors. However, as the authors have shown, the errors of the method are large due to spectral width of the CERES window channel. The first attempt at using ANN for both SW and LW TOA flux retrievals, Loukachine and Loeb (2003), relied on a multi-layer perceptron technique for TOA flux estimation from CERES measurements on the Tropical Rainfall Measuring Mission (TRMM) satellite. The ANN-based ADMs were developed for tropical regions using eight months of available data for neural network training. That study demonstrated that the CERES/TRMM ANN-based models are more accurate than ERBE ADMs for mean regional TOA flux estimation. It was also shown that both SW and LW ANN-derived fluxes have smaller residual dependence on CERES viewing zenith angle than the ERBE-like fluxes.

In this paper, we further develop the application of ANN simulation to the TOA radiative flux retrievals from CERES/*Terra* measurements in the absence of coincident imager information. A global set of SW, LW, and WN ANN-based ADMs is developed for ten sur-

face types using a complete year of CERES/*Terra* data. A partially-connected feed-forward error-backpropagation network simulation is applied in combination with compact low-noise training sets for the ANN performance optimization. To demonstrate the accuracy of the method we compare the ANN-derived results with the original CERES/*Terra* TOA flux values. Because of similarity in results for LW and WN we discuss results only for SW and LW TOA fluxes.

2. Observations

Two identical instruments, CERES Flight Model 1 (FM-1) and 2 (FM-2), were launched into a descending sun-synchronous orbit on the *Terra* satellite in December 1999. Each instrument has a spatial resolution of approximately 20 km at nadir (equivalent diameter) and scans the Earth over the full range of viewing zenith angle (VZA). CERES operates in three scanning modes - across the satellite ground track (cross-track), along the direction of the satellite ground track (along-track), and in a Rotating Azimuth Plane (RAP). In RAP mode, the radiometers scan in elevation as they rotate in azimuth, thus acquiring radiance measurement from a wide range of viewing angles. One CERES instrument scans in cross-track mode while the other is in RAP or along-track mode. The instrument operating in RAP scanning mode takes two days of along-track data every month.

For this study we use the CERES/*Terra* FM-1 and FM-2 Single Scanner Footprint (SSF) dataset for 2001. The SSF product contains coincident CERES and MODIS measurements. The MODIS scans in a cross-track mode up to 63° in VZA. Only CERES footprints that at least partially lie in the MODIS swath are retained in the SSF product. Therefore, the CERES footprints with VZA larger than 63° appear only when CERES is in the RAP or along-track scan modes.

Total fraction A_{unk} of area with unknown cloud properties over CERES footprint is determined by combining the imager coverage A_{im} and the fraction A_{ncl} of the cloudy area lacking cloud properties as follows:

$$A_{unk} = (1 - A_{im}) + A_{im}(1 - A_{clr})A_{ncl} , \quad (1)$$

where the first term provides the fraction of the footprint with no imager coverage, and the second term is the fraction of the footprint from the cloudy area with unknown cloud properties. The original CERES/*Terra* ADMs are developed and applied to the footprints with $A_{unk} < 35\%$, Loeb et al. (2003). Approximately 5.6% of CERES footprints in the 2001 dataset lack sufficient imager information, $A_{unk} > 35\%$, to provide scene identification. The regional frequency of these CERES footprints is shown in Fig. 1 for CERES/*Terra* data from 2001, with CERES in RAP scanning mode. The frequency is a strong function of the imager viewing geometry, surface and cloud conditions, and geography. Regionally, it can reach up to 50% over fresh snow (North Canada), sea-ice (sea of Okhotsk and Antarctica ice-shelf), mountainous (Tibet) or coastal regions (Arabian peninsula). Difference in surface conditions creates a large difference in sampling, as it is in the case of Greenland (permanent snow) and Arctic ocean (sea ice). Footprints with thin high cloud layers also frequently lack imager cloud

property coverage due to rejection by the imager cloud algorithms, Minnis et al. (1999). When CERES radiometers are in the cross-track mode, footprints on the edges of the swath often lack sufficient imager pixel coverage to provide scene identification over entire field-of-view.

In addition to CERES and MODIS, the SSF dataset also includes meteorological data based on the Global Modeling and Assimilation Office (GMAO)’s Goddard Earth Observing System DAS (GEOS-DAS V4.0.3) product, DAO (1996). The GMAO provides parameters such as surface skin temperature, precipitable water, and column averaged relative humidity. A comprehensive description of all parameters appearing in CERES/*Terra* SSF datasets is provided in the CERES Collection Guide, Geier et al. (2003).

3. ANN Method and Training Results

To obtain the ANN-derived CERES TOA fluxes, we use CERES data with coincident MODIS information to train neural networks to reproduce the original scene-dependent CERES/*Terra* ADM as five-dimensional function of variables, $v_1...v_5$. This set of variables is available with the CERES measurement alone: viewing zenith angle (VZA), relative azimuth (RAZ), LW broadband radiance (LWR), solar zenith angle (SZA), SW broadband radiance (SWR). The ANN-based ADM is then applied to convert CERES broadband radiances into TOA fluxes using the following

$$F_{ANN} = \frac{\pi I}{R_{ANN}(v_1...v_5)} , \quad (2)$$

where F_{ANN} is the ANN-derived TOA flux, I and $R_{ANN}(v_1...v_5)$ are the measured broadband radiance and ANN-based ADM, respectively. To reproduce the original CERES/*Terra* ADMs we use feed-forward error-back-propagation multi-layer ANN simulation technique. This type of neural network is a well-known tool for creating highly non-linear, multi-dimensional, continuous transfer functions, Hagan et al. (1996) and Aires et al. (2001). For ANN training we use the method described in Loukachine and Loeb (2003) with a few modifications, which we discuss below.

3.1. ANN Layout

The ANN layout is shown in Fig. 2. For the shortwave ADMs the ANN input variables are: CERES VZA, RAZ, LWR, SZA, and SWR, as shown in Fig. 2. The first and second hidden neuron layers, L^1 and L^2 , consist of neurons with a tangent sigmoid activation function, and the output neuron, L^3 , has a linear activation function. In order to avoid operations with large numbers, all inputs to the network are normalized to the maximum allowable value for each variable: $300 \text{ Wm}^{-2}\text{sr}^{-1}$ for SWR, $150 \text{ Wm}^{-2}\text{sr}^{-1}$ for LWR, 90° for both SZA and VZA, and 180° for RAZ¹. The upper limits for SWR and LWR define the variable range with sufficient CERES/*Terra* SSF data for network training, and the ANN is not to be used beyond these limits. The normalization process is indicated by letter N in Fig. 2. Neurons in the first hidden

¹Normalization factor for precipitable water, used in LW and WN ANNs, is 10 cm. Normalization factor for SZA is 180° for night data.

neuron layer, L^1 , are divided into two groups, each dedicated to specific variables. The reason for this partial connectivity is to separate weakly and strongly correlated input parameters. The first group of four neurons is connected to only three input variables: viewing zenith angle, relative azimuth angle, and longwave radiance. The second group of three neurons is connected to the other two variables for which the SW flux is strongly dependent: shortwave radiance and solar zenith angle. The LW day- and night-time use the same structure for the first hidden neuron layer. The second hidden neuron layer, L^2 , consists of 11 neurons for SW and 9 neurons for LW ANNs. They are uniformly connected to all the neurons in the first and third neuron layers. Input variables for SW, LW day- and night-time ANNs are shown in Table 1. We note that in the case of the LW networks, in addition to information provided by CERES, we use precipitable water (PW), provided by GMAO, as the ANN input variable.

3.2. Training Sets

Generally, neural network simulation involves three steps: (i) definition of the training sets; (ii) neural network training; and (iii) application of the network to data of interest. To create the ANN training sets, we use the entire year of 2001 SSF data with CERES in RAP scanning mode. Only CERES footprints with sufficient MODIS information, $A_{unk} < 35\%$, are considered.

Although computation time limits the size of a training set, the training set must be large enough to represent the complexity of the data in order to allow the ANN function to generalize well, Bose and Liang (1996). First, we define ten surface scene types based on the International Geosphere Biosphere Programme (IGBP) surface map, Geier et al. (2003), as shown in Table 2. For every surface scene type, the CERES SSF data is then independently stratified by five input variables. The variables, number of bins and bin-widths for SW, LW day- and night-time training sets are shown in Table 1. For each five-dimensional configuration we compute the mean and standard deviation (STD) of the original CERES/*Terra* ADM values, and the mean values of each input variable. These are the constituents of the ANN training sets. By requiring a minimum number of CERES footprints per configuration, we reduce the data to compact sets of approximately 15,000 configurations for land scene types, and 25,000 configurations for the Water Bodies scene type. Because of differences in sampling rate, these numbers vary from one scene type to another for SW and LW training sets. By applying a constant statistic threshold to all configurations within a training set we assure representation of high density data, and therefore good ANN training results for the bulk of the data. Further, to reduce data noise we set an upper-limit on the STD value of the ADM distribution within a training configuration. The exclusion of noisy configurations from the training sets is illustrated in Fig. 3 for SW training sets: Water Bodies (Fig. 3a) and Dark Desert (Fig. 3b) as an example for a land scene. The STD(ADM) upper-limit for SW training sets is 8.0% for all scene types. The STD(ADM) upper-limits for LW day- and night-time training sets are 2.0% and 3.0%, respectively. The noisy data configurations, with STD(ADM) exceeding the limits, are archived during this procedure. They amount to approximately 2-3% of the total number for the land, snow and ice, and about 10% for Water Bodies training sets. Because of sun glint over water surface, large number of the noisy configurations for the Water Bodies SW training set come from the CERES viewing geometry with small glint angles (Fig.

3a). For the land scene types distribution of the noisy configurations is relatively uniform in all variables. Thus, we have thirty compact low-noise ANN training sets for ten scene types for SW, LW day- and night-time CERES/*Terra* original ADMs.

3.3. ANN Training

Having constructed the training sets, we then train the ANNs using the Generalized Delta rule with a varying learning rate and a constant momentum, Hagan et al. (1996). To ensure smooth and effective ANN learning we define an error index over the entire training set as:

$$E(k) = \sum_{i=1}^N [t_i - \mathbf{a}_i^3(k)]^2, \quad (3)$$

where N is the number of configurations in a training set, t_i is the ADM target value (mean ADM value in a training configuration), and $\mathbf{a}_i^3(k)$ is the ANN output at iteration k . Thus, the error index is the sum of the square of errors from all training configurations, and is computed at the end of every learning iteration. If the error index decreases, a training iteration ends and the ANN connection weight and neuron bias values are updated as described in Loukachine and Loeb (2003). As a compromise between computation time and desirable accuracy, we used 10,000 iterations for all land, snow and ice ANN scene types. Because of its larger training set size, we used 15,000 iterations for the Water Bodies ANN scene type. The training process for Bright Desert SW ANN is illustrated in Fig. 4. With each iteration the error index monotonically decreases as shown in Fig. 4a. At the end of training, the ANN reproduces ADM values very closely for all configurations of the training set. A frequency distribution of the relative difference between ANN-derived and training set ADMs, $(R_{ANN} - R_{SET})/R_{SET}$, is shown in Fig. 4b. The mean and STD values of this distribution for the entire training set are selected as quantitative estimates of training success. Training results for SW, LW day- and night-time for all ANN scene types are shown in Table 2. The mean deviation from the target ADM values is very small for all ANN scene types. The average STD is approximately 3.5% for SW, and 1% for LW day- and night-time ANNs.

When the training is complete, the ANN connection weights and neuron biases are frozen, and the networks represented by the transfer functions, $R_{ANN}(v_1 \dots v_5)$ (Equation 1), are ready to be applied. To reduce overall error in ANN-derived fluxes the archived list of noisy configurations for every ANN scene type is used to reject noisy data.

4. Validation Results

4.1. ANN-derived Mean TOA flux

To validate ANN-based models we compare the ANN-derived and original CERES/*Terra* SSF fluxes. For this purpose we use CERES/*Terra* SSF data from 2001, the footprints with both the original CERES/*Terra* and ANN-based ADMs defined.

The global mean (bias) of the difference between the ANN-derived and original CERES/*Terra* TOA fluxes is shown in Table 3 for each ANN scene type. For SW, most of the ANN scene types have a small negative bias. Only Deciduous Forest and Dark Desert scene types have bias values that exceed 0.5%. For LW, the biases are also small for all scene types except Sea Ice at night and Snow and Sea Ice for both day and night. For these scene types the bias is about 0.7%. Since the overall sampling is dominated by ocean, the global bias value is within 0.2% for both SW and LW TOA fluxes.

Figure 5 shows regional differences between mean all-sky ANN-derived and original CERES/*Terra* fluxes for SW (Fig. 5a), LW day-time (Fig. 5b) and LW night-time (Fig. 5c) data. Locally, the maximum differences are within 10 Wm^{-2} and 3 Wm^{-2} for SW and LW, respectively. While the global bias is relatively small the ANN shows significant errors over snow and sea ice surfaces, particularly in the polar regions where the fraction of CERES footprints without imager-based scene ID is large (see Fig. 1). For LW at night, the ANN function also shows larger errors over West Tropical Pacific ocean region, where precipitable water is large. We believe, improvements in ANN performance in these regions can be achieved by artificially increasing the density of configurations with large mean values of precipitable water in the Water Bodies training set.

The expected minimum STD value of the difference between the ANN-derived and original CERES/*Terra* TOA fluxes for a scene type, STD_{MIN} , can be estimated as:

$$STD_{MIN} = \sqrt{\overline{STD(ADM)}^2 + STD_T^2}, \quad (4)$$

where $\overline{STD(ADM)}$ is the $STD(ADM)$ average over a training set, and represents the intrinsic uncertainty of the target ADMs. The STD_T is the STD of the relative difference between ANN-based and target ADMs after the training is complete (see Table 2). The STD_{MIN} and STD of the difference between the ANN-derived and original CERES/*Terra* TOA fluxes for 2001 data are shown in Table 3. The STD_{MIN} and STD values agree within less than one per cent for SW and a few tenth of a per cent for LW for all ANN scene types. This result is very important as it illustrates the motivation for our approach used to create training sets: average of the original CERES/*Terra* ADMs using a large dataset and calculate $STD(ADM)$ for every training configuration. Using these together with STD_T , we are able estimate the errors in the method and have a reliable consistency control.

The comparison of the all-sky mean SW TOA flux stratified by solar zenith angle is shown in Fig. 6a. The ANN-based fluxes reproduce the original CERES/*Terra* fluxes on average to within 2 Wm^{-2} for all SZA values except for $SZA < 10^\circ$, where the difference is about 15 Wm^{-2} . This small SZA range data is poorly sampled because *Terra* is in a 10:30 a.m. sun-synchronous orbit, and because of SW training configuration rejection due to large noise in the original CERES/*Terra* ADMs (sun glint over ocean, see Fig. 3a). The situation is very similar in LW case. The comparison of the all-sky mean LW TOA fluxes stratified by precipitable water is shown in Fig. 7a and Fig. 8a for day and night CERES data, respectively. The ANN-derived TOA fluxes reproduce the original ADM fluxes, within 2 Wm^{-2} for all PW

values except $PW > 8$ cm, where the sampling is poor. For $PW > 8$ cm, the difference is approximately 3 Wm^{-2} and 4 Wm^{-2} for LW day- and night-time, respectively. To reduce errors when data sampling is poor, the number of these particular data configurations should be artificially increased in the training sets by reducing the statistical threshold.

4.2. Instantaneous Flux Consistency

From its definition, TOA flux should not depend on satellite viewing geometry. Thus, a difference in instantaneous TOA flux values at different viewing angles over the same scene can be used for estimating instantaneous flux consistency. We note, that *consistency* is not a guarantee of absolute accuracy since the true flux from the scene is unknown. However, in this study we are interested in a relative comparison between the original CERES/*Terra* SSF and ANN-derived TOA flux errors.

Forty days of along-track and coincident cross-track CERES/*Terra* SSF data from 2001 and 2002 are used to estimate instantaneous TOA flux consistency. The Earth's surface is divided into regions of 1° longitude and 0.02 in $\sin(\text{latitude})$. In the cross-track scanning mode, CERES and MODIS view a footprint at the same angle, and so that a linear regression from instantaneous MODIS narrowband to CERES broadband radiance can be derived for every region. We retain only the regressions for regions containing at least 25 CERES footprints, where the bias in the linear fit is less than $10^{-4}\%$ and the relative STD is smaller than 3% for SW, and 1% for LW day- and night-time. These linear functions are applied to coincident data with CERES in along-track mode to derive near-nadir broadband radiances for every CERES footprint in the region. During this procedure all measurements within a region are time-matched within 2 minutes in order to ensure consistency of the atmospheric conditions. With all statistical requirements we have 64,728 regions for SW, 94,788 and 134,657 regions for LW day- and night-time data, respectively. These regions are distributed over all longitude and latitude range.

In the along-track scanning mode a footprint is viewed by the CERES at various viewing zenith angles, θ , and by MODIS at an angle close to nadir. First, previously obtained linear regression in the region is used to calculate the nadir broadband radiance from the MODIS narrowband radiance over the CERES footprint. Then, CERES and near-nadir broadband radiances are converted into TOA fluxes using the CERES or ANN-based ADMs according to Equation 1. We define instantaneous flux consistency as *RMS* of the difference between CERES TOA fluxes at large, θ , and near-nadir, θ_{NN} , viewing zenith angles with condition that $50^\circ < \theta - \theta_{NN} < 60^\circ$:

$$RMS = \sqrt{\frac{\sum_{i=1}^N [F_i(\theta) - F_i(\theta_{NN})]^2}{N}}, \quad (5)$$

where N is the number of CERES footprints, $F_i(\theta)$ and $F_i(\theta_{NN})$ are fluxes at large and near-nadir viewing zenith angles respectively. This procedure is applied for both the original CERES/*Terra* and ANN-based models.

Global average all-sky relative *RMS* values for all ANN scene types are shown in Table 3 for SW, LW day- and night-time. Average *RMS* level for SW and LW reflects the allowed noise upper-limits in the ANN training sets. The difference between ANN scene types is due to the difference in complexity of transfer functions and degree of ANN generalization. In average ANN-derived TOA fluxes are instantaneously consistent within 9% for shortwave, 3.5% and 3% longwave day- and night-time, respectively.

The comparison of instantaneous consistency for the CERES/*Terra* and ANN-based ADMs is shown in Fig. 6b, Fig. 7b and Fig. 8b, where the mean RMS values are plotted versus $\sin(\text{latitude})$. LW day-time (Fig. 7b) and night-time (Fig. 8b) ANN-derived fluxes have instantaneous consistency that is very close to the CERES/*Terra* fluxes. Compared with the original CERES/*Terra* TOA fluxes, global average *RMS* for ANN-based TOA fluxes are factor 1.33 larger for SW, factor 1.25 for LW night-time, and practically comparable for LW day-time data.

Using cloud information over CERES footprints inferred from MODIS, Minnis et al. 2003, we find that instantaneous consistency errors for SW and LW night-time ANN-derived fluxes are generally larger than for the original CERES/*Terra* fluxes for scenes with thin high altitude cloud layers. As in the case of data with small SZA and large precipitable water, this is, again, a case where data sampling is poor, and therefore not well-represented in the training sets.

5. Summary and Conclusions

Using artificial neural network (ANN) approach, we developed a complete global set of angular distribution models (ADMs) for TOA flux retrievals from CERES measurement alone. Trained on CERES/*Terra* SSF dataset, the SW, LW, and WN ANN-based ADMs are built for ten surface types, and represent five-dimensional continuous functions. Close reproduction of the original CERES/*Terra* ADMs is achieved by using a partially connected feed-forward error-backpropagation ANN structure in combination with low-noise compact training sets. These models are applied to CERES/*Terra* data with insufficient imager information for scene identification, and play an important role in regions where the fraction of such data with insufficient is relatively large: coastal Antarctica, mountainous regions of Asia, equatorial Africa, sea-ice and fresh snow surfaces.

When compared with the original CERES/*Terra* TOA fluxes the ANN-derived mean TOA fluxes show a very small global deviation for all scene types. Maximum regional mean ANN flux deviation from the original fluxes is less than 10 Wm^{-2} for SW, and less than 2 Wm^{-2} for LW data. The largest difference occurs in polar regions over sea ice and permanent snow surfaces. When stratified by solar zenith angle and precipitable water, mean SW and LW TOA fluxes are reproduced to within of 2 Wm^{-2} , except in areas of poorly sampled data with $\text{SZA} < 10^\circ$ and $\text{PW} > 8 \text{ cm}$. These results confirm that the method allows good neural network generalization during the training phase. For all ANN scene types, the STD of the difference between the ANN-derived and CERES/*Terra* SSF TOA fluxes are in a very good agreement with the expected values.

For all surface types, ANN-derived TOA fluxes are instantaneously consistent in VZA to within 9% for SW, 3.5% and 3% LW day- and night-time, respectively. This is about factor 1.33 and 1.25 larger than that of the CERES/*Terra* for SW and LW night-time, and practically comparable for LW day-time. Instantaneous TOA flux consistency of the ANN-based TOA fluxes are generally larger for poorly sampled scene types, such as high altitude thin cloud layers.

Further improvement in ANN performance and reduction of ANN-derived TOA flux errors for poorly sampled data can be achieved by increasing its density in the training sets artificially. The ANN-based ADMs are accessible interactively at the CERES Inversion Group official web-site, <http://asd-www.larc.nasa.gov/Inversion/adm/>.

Acknowledgments

The authors would like to thank Sandra K. Nolan of Science Applications International Corporation for producing the CERES/*Terra* SSF subset. This research was funded by the Clouds and the Earth's Radiant Energy System (CERES) project under NASA Grant NNL-04AA26G.

References

- Aires, F., A. Chedin, N.A. Scott and W.B. Rossow (2001), A Regularized Neural Net Approach for Retrieval of Atmospheric and Surface Temperatures with the IASI Instrument. *J. Appl. Meteor.*, 41, 144-159.
- Barkstrom, B.R. (1984), The Earth Radiation Budget Experiment. *Bull. Amer. Meteorol. Soc.*, 65, 1170-1186.
- Bose, N.K., and Liang, P. (1996), *Neural Network Fundamentals with Graphs, Algorithms, and Applications*. McGraw-Hill Electrical and Computer Engineering Series.
- DAO (1996), Algorithm Theoretical Basis Document for Goddard Earth Observing System Data Assimilation System (GEOS DAS) with a focus on version 2. Available online at <http://dao.gsfc.nasa.gov/subpages/atbd.html>
- Geier, E.B., R.N. Green, D.P. Kratz, P. Minnis, W.F. Miller, S.K. Nolan, and C.B. Franklin (2003), Single Satellite Footprint TOA/surface Fluxes and Clouds (SSF) Collection Guide Document. Available online at http://asd-www.larc.nasa.gov/ceres/collect_guide/
- Hagan, M.T., Demuth, H.B. and Beale, M.H. (1996), *Neural Network Design*. Brooks/Cole Pub. Co.
- Loeb, N.G., N. Manalo-Smith, S. Kato, W.F. Miller, S. Gupta, P. Minnis, and B. Wielicki (2003), Angular distribution Models for Top-of-Atmosphere Radiative Flux Estimation from

the Clouds and the Earth's Radiant Energy System Instrument on the Tropical Rainfall Measuring Mission Satellite, Part I: Methodology. *J. Appl. Meteor.*, 42, 240-265.

Loeb, N.G., S. Kato, K. Loukachine, N. Manalo-Smith (2004), Angular Distribution Models for Top-of-Atmosphere Flux Estimation from the Clouds and the Earth's Radiant Energy System Instrument on Terra Satellite. Part I: Methodology. Submitted in *J. of Atm. and Oce. Tech.*

Loukachine, K. and Loeb N.G. (2003), Application of an Artificial Neural Network Simulation for Top-of-Atmosphere Radiative Flux Estimation from the Clouds and the Earth's Radiant Energy System (CERES). *J. of Atm. and Oce. Tech.*, 20, No. 12, 1749-1757.

Minnis, P., D. F. Young, B. A. Wielicki, P. W. Heck, X. Dong, L. L. Stowe, R. Welch (1999), CERES Cloud Properties Derived From Multispectral VIRS Data. Proc. The EOS/SPIE Symposium on Remote Sensing, vol. 3867, Florence, Italy, September 20-24, 91-102.

Minnis, P., D.F. Young, S. Sun-Mack, P.W. Heck, D.R. Doelling, and Q. Trepte (2003), CERES Cloud Property Retrievals from Imager on *TRMM*, *Terra* and *Aqua*, Proc. SPIE 10th International Symposium on Remote Sensing: Conference on Remote Sensing of Clouds and the Atmosphere VII, Barcelona, Spain, September 8-12, 37-48.

Stubenrauch, C.J., J.P. Duvel, R.S. Kandel (1993), Determination of Longwave Anisotropic Emission Factors from Combined Broad- and Narrowband Radiance Measurements. *J. Appl. Meteor.*, 32, 848-856.

Wielicki, B.A., R.D. Cess, M.D. King, D.A. Randall, and E.F. Harrison (1995), Mission to Planet Earth: Role of Clouds and Radiation in Climate. *Bull. Amer. Meteor. Soc.*, 76, 2125-2152.

Wielicki, B.A., B.R. Barkstrom, E.F. Harrison, R.B. Lee III, G.L. Smith, and J.E. Cooper (1996), Clouds and the Earth's Radiant Energy System (CERES): An Earth Observing System Experiment. *Bull. Amer. Meteor. Soc.*, 77, 853-868.

TABLE 1. ANN input variables and stratification of the CERES/*Terra* SSF data for building SW, LW day- and night-time training sets. Units of the bin-width, Δ -Bin, are $\text{Wm}^{-2}\text{sr}^{-1}$ for radiance (SWR, LWR), degrees for angles (VZA, SZA, RAZ), and cm for precipitable water (PW).

	Variable SW	N Bins SW	Δ -Bin SW	Variable LW DAY	N bins LW DAY	Δ -Bin LW DAY	Variable LW NIGHT	N bins LW NIGHT	Δ -Bin LW NIGHT
1	VZA	7	10.0	VZA	7	10.0	VZA	7	10.0
2	RAZ	9	20.0	RAZ	6	30.0	RAZ	6	30.0
3	LWR	15	10.0	SWR	20	15.0	SZA	9	10.0
4	SZA	9	10.0	PW	10	1.0	PW	10	1.0
5	SWR	30	10.0	LWR	30	5.0	LWR	40	3.0

TABLE 2. Definition of ANN scene types using IGBP: Evergreen Forests (EF), Deciduous Forests (DF), Woody Savannas and Shrublands (WS), Dark Desert (DD), Bright Desert (BD), Water Bodies (WB), Grasslands (GR), Croplands and Cities (CC), Permanent and Fresh Snow (SN), Sea Ice (SI). Bias and STD_T of the relative difference between the ANN-based and target ADMs after the training for SW, LW day and night.

ANN Scene	IGBP Types	Bias SW (%)	STD_T SW (%)	Bias LW Day (%)	STD_T LW Day (%)	Bias LW Night (%)	STD_T LW Night (%)
EF	1, 2	0.11	3.42	0.011	0.98	0.023	1.48
DF	3, 4, 5	0.15	3.87	0.007	0.81	0.013	1.02
WS	6, 8	0.13	3.57	0.011	0.91	0.028	1.66
DD	7, 18	0.11	3.50	0.006	0.72	0.015	1.09
BD	16	0.08	2.97	0.008	0.67	0.017	1.20
WB	17	0.13	4.06	0.010	0.91	0.010	0.93
GR	9, 10, 11	0.12	3.48	0.010	0.90	0.021	1.37
CC	12, 13, 14	0.12	3.41	0.009	0.85	0.014	1.15
SN	15, 19	0.12	3.66	0.013	1.02	0.012	1.05
SI	20	0.12	3.83	0.005	0.62	0.006	0.83

TABLE 3. Mean (bias), STD , and expected minimum STD_{MIN} of the difference between the ANN-derived and original CERES/*Terra* TOA fluxes. The STD and STD_{MIN} are shown as superscript and subscript to the bias values, respectively. The ANN-derived TOA flux instantaneous consistency, RMS , for all ANN scene types.

ANN Type	BIAS $\overset{STD}{\underset{STD_{MIN}}{SW}}$ (%)	BIAS $\overset{STD}{\underset{STD_{MIN}}{LW Day}}$ (%)	BIAS $\overset{STD}{\underset{STD_{MIN}}{LW Night}}$ (%)	RMS SW (%)	RMS LW Day (%)	RMS LW Night (%)
EF	-0.28 $\overset{5.13}{\underset{4.48}{}}$	-0.13 $\overset{1.52}{\underset{1.27}{}}$	-0.08 $\overset{1.99}{\underset{1.91}{}}$	8.89	4.35	3.71
DF	-0.68 $\overset{5.96}{\underset{5.05}{}}$	-0.14 $\overset{1.33}{\underset{1.15}{}}$	-0.21 $\overset{1.69}{\underset{1.49}{}}$	10.14	4.15	3.56
WS	-0.33 $\overset{5.64}{\underset{4.64}{}}$	-0.08 $\overset{1.40}{\underset{1.23}{}}$	-0.03 $\overset{1.95}{\underset{2.14}{}}$	9.10	4.36	3.75
DD	-0.51 $\overset{5.78}{\underset{5.04}{}}$	-0.10 $\overset{1.23}{\underset{1.16}{}}$	-0.38 $\overset{1.68}{\underset{1.65}{}}$	9.22	3.90	2.98
BD	-0.12 $\overset{4.77}{\underset{4.21}{}}$	-0.01 $\overset{0.97}{\underset{1.02}{}}$	-0.25 $\overset{1.51}{\underset{1.91}{}}$	7.18	3.09	2.65
WB	0.02 $\overset{5.93}{\underset{5.29}{}}$	-0.21 $\overset{1.20}{\underset{1.24}{}}$	-0.11 $\overset{1.41}{\underset{1.62}{}}$	9.33	3.68	2.83
GR	-0.10 $\overset{5.36}{\underset{4.73}{}}$	-0.13 $\overset{1.46}{\underset{1.29}{}}$	-0.24 $\overset{1.86}{\underset{1.95}{}}$	9.70	4.30	3.44
CC	-0.15 $\overset{5.35}{\underset{4.68}{}}$	-0.17 $\overset{1.53}{\underset{1.20}{}}$	-0.26 $\overset{1.90}{\underset{1.69}{}}$	9.71	4.54	3.54
SN	-0.18 $\overset{5.25}{\underset{5.30}{}}$	-0.68 $\overset{1.45}{\underset{1.31}{}}$	-0.39 $\overset{1.99}{\underset{1.50}{}}$	8.90	3.60	3.22
SI	0.11 $\overset{6.38}{\underset{5.71}{}}$	-0.65 $\overset{0.92}{\underset{0.84}{}}$	-0.70 $\overset{1.19}{\underset{1.05}{}}$	10.84	3.32	3.36

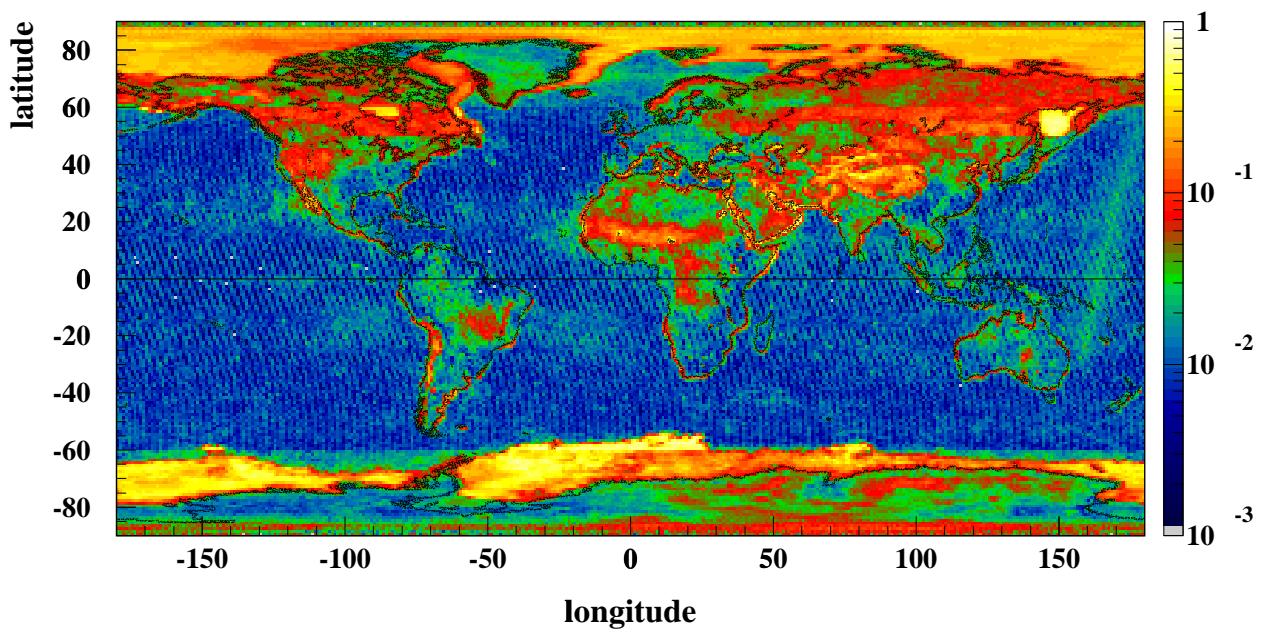


Figure 1: Fraction of CERES footprints lacking imager information for a reliable scene identification.

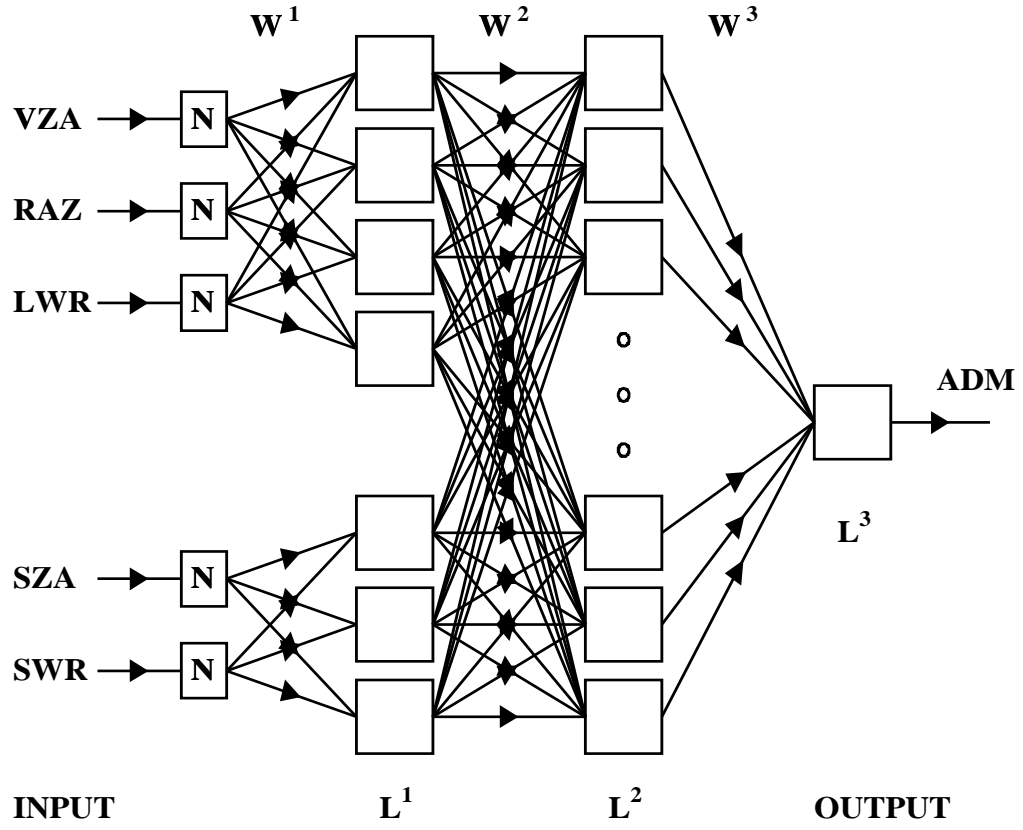


Figure 2: Layout of the ANN used in this study. Open rectangles show the neurons, which form two hidden layers, L^1 and L^2 , and an output layer, L^3 . The ANN inputs are partially connected with the first hidden neuron layer, L^1 . Input normalization process shown with rectangles containing letter N . The weighted connections between neurons are denoted as W^1 , W^2 and W^3 .

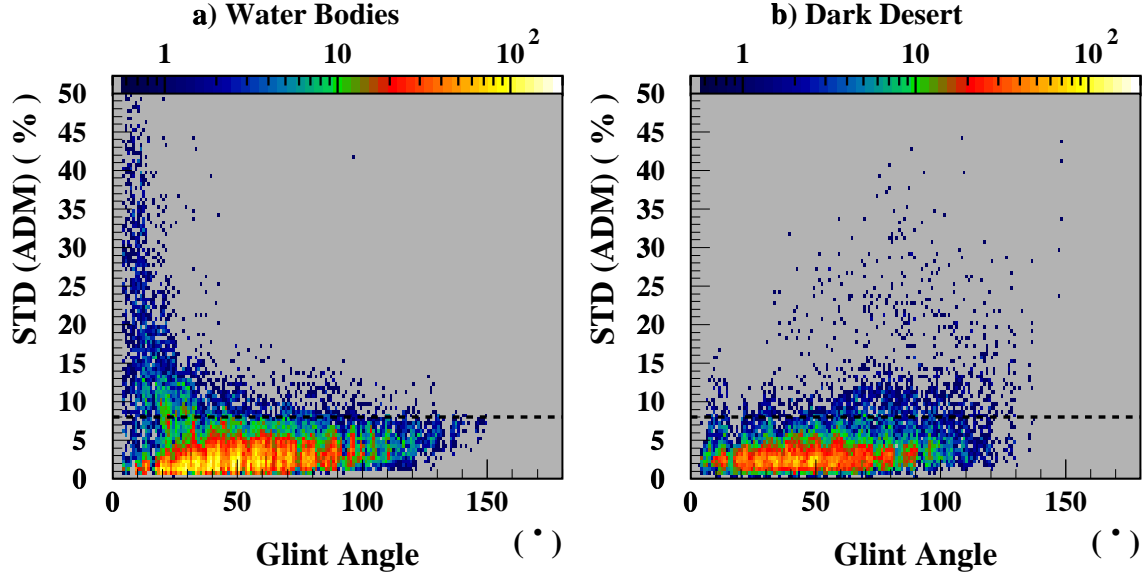


Figure 3: SW ANN training sets: frequency distribution of the training configurations in relative STD(ADM) and in mean glint angle for a) Water Bodies scene type, ADM noise increase considerably at small glint angle; and b) Dark Desert surface type. Dashed line shows the allowed upper-limit of $\text{STD(ADM)} = 8.0\%$.

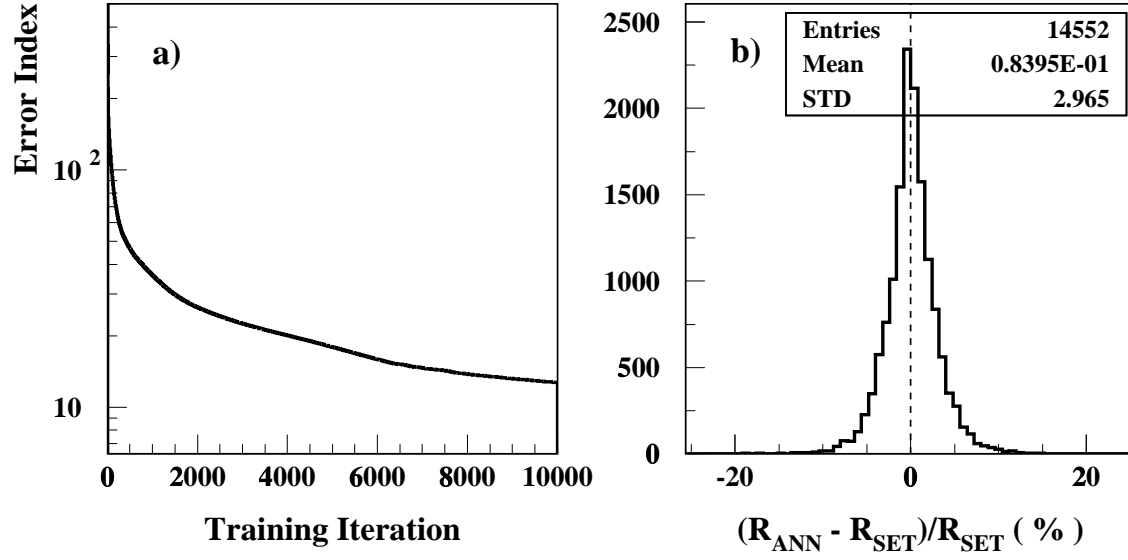


Figure 4: SW ANN training for Bright Desert scene type: a) Error index decreases with training iteration, b) Frequency distribution of the relative difference between ANN-derived, R_{ANN} , and training set ADM values, R_{SET} .

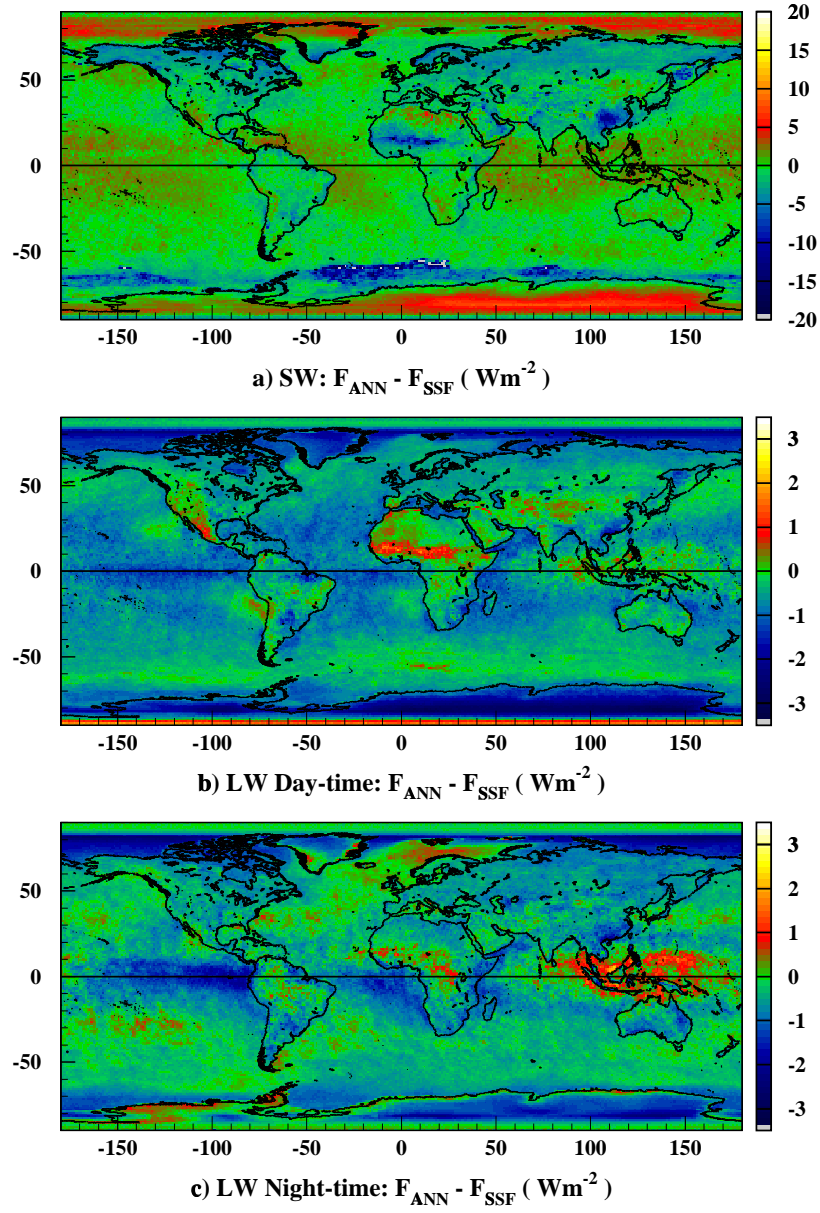


Figure 5: Regional difference between mean ANN-derived and the original CERES/*Terra* SSF fluxes: a) SW, b) LW day-time, and c) LW night-time.

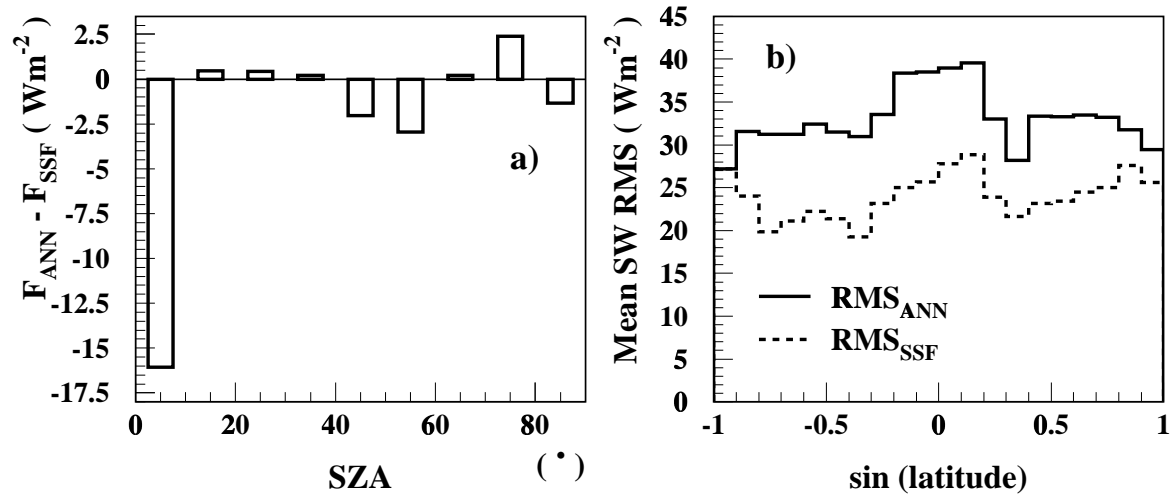


Figure 6: Validation of the SW ANN-based ADMs: a) Difference between mean SW ANN-derived and original CERES/*Terra* SSF fluxes versus SZA. b) Instantaneous mean SW flux RMS versus sin(latitude) for ANN-based (solid line) and the original CERES/*Terra* SSF (dashed line) ADMs.

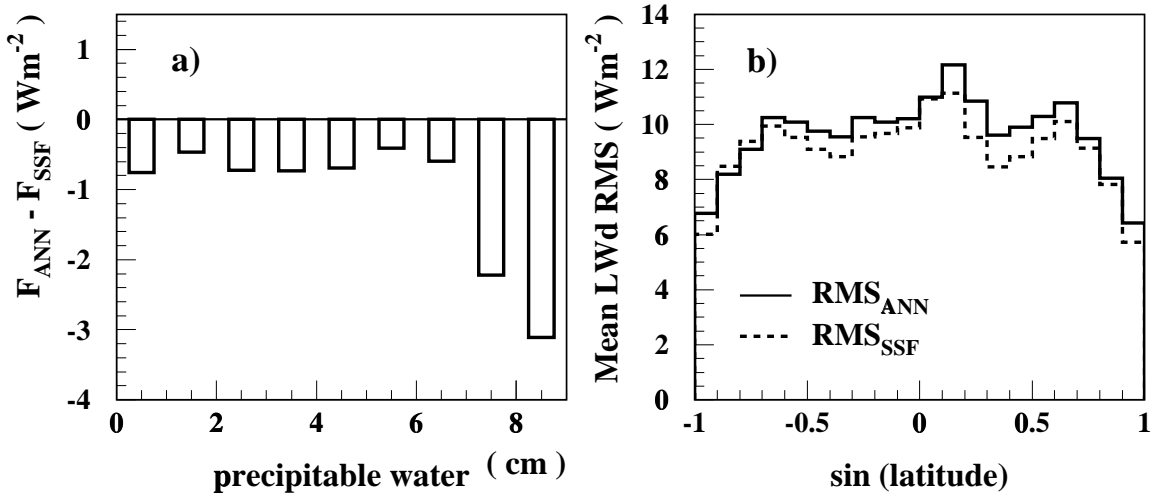


Figure 7: Validation of the LW day-time ANN-based ADMs: a) Difference between mean LW day-time ANN-derived and original CERES/*Terra* SSF fluxes versus precipitable water. b) Instantaneous mean LW day-time flux RMS versus $\sin(\text{latitude})$ for ANN-based (solid line) and original CERES/*Terra* SSF (dashed line) ADMs.

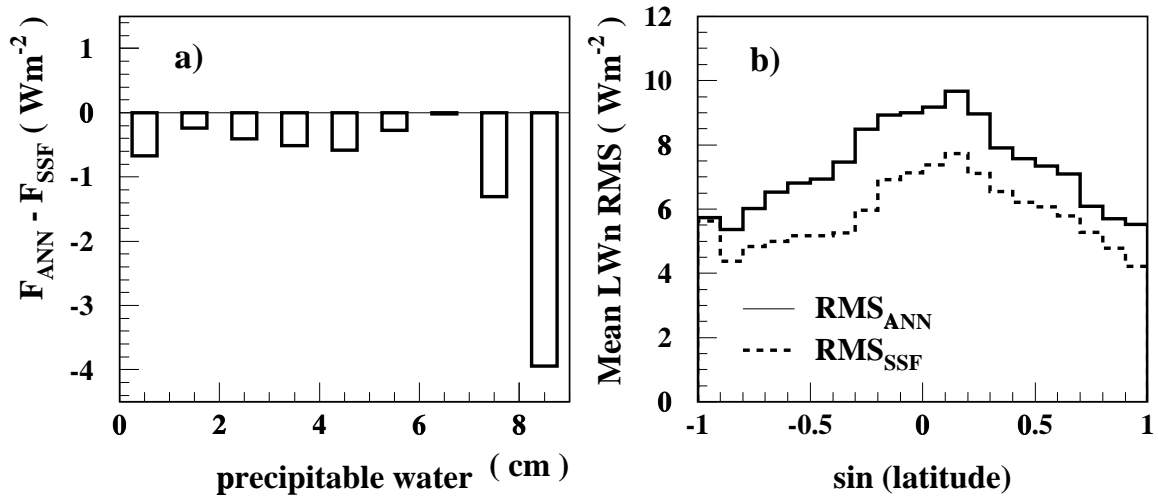


Figure 8: Validation of the LW night-time ANN-based ADMs: a) Difference between mean LW night-time ANN-derived and original CERES/*Terra* SSF fluxes versus precipitable water. b) Instantaneous mean LW night-time flux RMS versus $\sin(\text{latitude})$ for ANN-based (solid line) and original CERES/*Terra* SSF (dashed line) ADMs.